Brittle yielding of amorphous solids at finite shear rates

Murari Singh,[1] Misaki Ozawa,[1,2] and Ludovic Berthier [1,3]

[1]*Laboratoire Charles Coulomb, UMR 5221 CNRS-Université de Montpellier, Montpellier 34095, France*
[2]*Département de Physique, Ecole Normale Supérieure, Paris 75005, France*
[3]*Department of Chemistry, University of Cambridge, Lensfield Road, Cambridge CB2 1EW, United Kingdom*

Amorphous solids display a ductile to brittle transition as the kinetic stability of the quiescent glass is increased, which leads to a material failure controlled by the sudden emergence of a macroscopic shear band in quasistatic protocols. We numerically study how finite deformation rates influence ductile and brittle yielding behaviors using model glasses in two and three spatial dimensions. We find that a finite shear rate systematically enhances the stress overshoot of poorly annealed systems, without necessarily producing shear bands. For well-annealed systems, the nonequilibrium discontinuous yielding transition is smeared out by finite shear rates and is accompanied by the emergence of multiple shear bands, as reported in metallic glass experiments. We show that the typical size of the bands and the distance between them increases algebraically with the inverse shear rate. We provide a dynamic scaling argument for the corresponding lengthscale, based on the competition between the deformation rate and the propagation time of the shear bands.

I. INTRODUCTION

The mechanical response of amorphous materials such as foams, colloids, and metallic glasses is an active research topic for material science, engineering, and for the physics of disordered systems [1–5]. Despite wildly different sizes and interactions of the constituent particles, these diverse materials show surprisingly universal rheological responses under external loadings, such as yielding, plastic rearrangements, avalanches, and shear bands. Concepts and ideas developed in statistical mechanics are thus particularly useful to extract and understand these universal features [4,5].

Here, we focus on the yielding transition of quiescent materials in shear start-up conditions. This problem addresses the basic question of how a given amorphous solid plastically deforms or break when a nonlinear mechanical deformation is applied by an external loading. In this setting, two types of yielding transitions can be observed. One type is brittle yielding, which is associated with an abrupt failure of the material and corresponds to the appearance of sharp shear bands [6]. The other is ductile yielding, which is accompanied by significant plastic deformations that prevent the emergence of a sharp failure and favor large deformations [4]. These different yielding behaviors may depend on material properties, preparation protocols, and loading conditions [7–18]. In particular, the initial stability of the glass (as controlled by the preparation protocol of the material) directly determines the brittle or ductile nature of yielding. More stable glasses show more brittle yielding, whereas less stable glasses demonstrate ductile behavior [12,14,15,17].

In the last decade, studies of yielding by the statistical physics community have been largely dedicated to steady-state properties after a large accumulated strain. Regarding shear start-up conditions, relatively poorly annealed glasses have been mostly analyzed, focusing on plastic

rearrangements [1,19,20], the formation of shear bands [12,21], and avalanche statistics [22–24]. Similar analysis and direct visualizations have also been performed in colloidal glasses [25,26]. Many useful concepts have emerged from these intensive investigations, from the definition of soft spots where plastic events successively take place [27–29] to the localization of shear deformation [30] and scaling laws for avalanche statistics [23,24,31].

By contrast, much less is known about the sharp yielding transition of brittle materials. This problem is, however, receiving growing attention thanks to the development of theoretical approaches [32–36] and progress in numerical techniques [37,38] that now allow the investigation of brittle yielding in atomistic computer simulations. From a theoretical viewpoint, brittle yielding under quasistatic loading corresponds to a nonequilibrium discontinuous transition. This is described as a spinodal transition in the mean-field limit [39], potentially avoided in finite dimensions [36]. In addition to these theoretical predictions, molecular simulations in athermal quasistatic shear (AQS) deformation [40] demonstrated that the nonequilibrium discontinuous transition can exist in finite-dimensional models, accompanied by the sudden appearance of a unique system-spanning shear band [36,41].

In the above studies, brittle yielding is described using the language of phase transitions and critical phenomena, but this description applies, strictly speaking, only in the AQS limit. In experiments, several additional factors may play a role and affect yielding, such as thermal fluctuations, spontaneous relaxation, inertia, and a finite deformation rate. In this paper, we deal with the latter and analyze the influence of a finite shear rate, leaving out temperature and inertia in this first effort. The loading rate dependence of yielding and the formation of shear bands is an important topic in material science and engineering [6,42], as well as soft matter [43]. In particular, it has been reported that multiple shear bands

appear at a higher strain rate in metallic glass experiments in various rheological conditions, and the density of shear bands increases with increasing $\dot{\gamma}$ [44–47]. Thus, a computational study about brittle yielding at finite $\dot{\gamma}$ provides useful microscopic insights for both experimental observations at higher strain rates [48] and for a fundamental understanding of the nature of the yielding transition [49]. Physically, we expect that the idealized picture of a single macroscopic shear band being responsible for the failure of the material cannot exist at finite shear rate, because it would take an infinite time to create an infinite shear band in an infinite system. The finite timescale introduced by the finite shear rate must compete with the propagation of shear bands. Our main goal is to understand the consequences of this competition and provide a real-space picture of how this affects yielding.

In this paper, we perform athermal, overdamped simulations at finite strain rate to shear glasses with a broad range of initial stabilities to characterize the relevant timescales and lengthscales associated with brittle yielding at finite strain rate. By measuring the stress-strain curve and associated susceptibilities, we find that the discontinuous yielding transition observed in the AQS simulations is smeared out in finite strain rate simulation, when $\dot{\gamma}$ is high and the system size N is large. Larger samples require slower $\dot{\gamma}$ to display brittle yielding with a single system spanning shear band. If $\dot{\gamma}$ is large for a given system size, we instead observe that multiple shear bands emerge, as reported in metallic glass experiments. We then extract a typical lengthscale ξ characterizing the spatial pattern of shear bands for a given $\dot{\gamma}$. We find that ξ scales as $\xi \propto \dot{\gamma}^{-\alpha}$, where $\alpha \approx 0.4$ for two-dimensional stable glasses. Thus, the lengthscale ξ diverges in the AQS limit, for sufficiently stable glasses. We argue that the observed scaling behavior can be understood as the competition between the deformation rate and the timescale associated with shear band formation.

This paper is organized as follows. In Sec. II, we describe the numerical methods. In Sec. III, we present the macroscopic rheological properties of glasses prepared with different initial stabilities to expose the basic differences between ductile and brittle yielding at finite strain rates. Section IV describes the effect of the finite strain rate on the nature of the yielding transition. The relevant lengthscale for the yielding transition is visualized and quantified in Sec. V. Finally, we discuss our results and conclude in Sec. VI.

II. NUMERICAL METHODS

A. Simulation models

We simulate size polydisperse systems of N particles in cubic and square boxes of length L in three (3D) and two (2D) dimensions using periodic boundary conditions. The pair interaction between particles i and j separated by a distance r_{ij} is a soft repulsive potential,

$$u(r_{ij}, d_{ij})/\epsilon = \left(\frac{d_{ij}}{r_{ij}}\right)^{12} + c_0 + c_2\left(\frac{r_{ij}}{d_{ij}}\right)^2 + c_4\left(\frac{r_{ij}}{d_{ij}}\right)^4,$$

$$d_{ij} = \frac{d_i + d_j}{2}(1 - 0.2|d_i - d_j|),$$

where r_{ij} is the distance between particles i and j, d_i is the diameter of the particle i, and ϵ is the energy scale. The set of parameters, c_0, c_2, and c_4, are adjusted so the potential and its first and second derivatives vanish at the cutoff distance $r_{\text{cut},ij} = 1.25d_{ij}$. The particle diameters are drawn randomly from a continuous size distribution $P(d) = A/d^3$ in the range $[d_{\min}, d_{\max}]$, where A is normalizing constant. We use parameters such that $d_{\min}/d_{\max} = 0.45$ and the average size diameter is $\bar{d} = 1.0$. We perform simulations at constant number density $\rho = 1.02$ for 3D, and $\rho = 1$ for 2D, using different system sizes $N \in [1500, 96\,000]$ in 3D and $N = 64\,000$ in 2D.

To prepare the glassy samples to be sheared at temperature $T = 0$, we first equilibrate the system at some finite temperature, T_{ini}, with the help of an efficient swap Monte Carlo method [37,50]. The equilibrium configurations are then instantaneously quenched at $T = 0$ using the conjugate gradient method [51]. We have checked that the minimization algorithm does not affect the rheological response of the system. We produce glassy samples using initial temperatures $T_{\text{ini}} \in [0.062, 0.200]$, which offers a broad range of kinetic stability. In 2D, the initial preparation temperatures are $T_{\text{ini}} \in [0.035, 0.200]$ [52]. For these temperature ranges, we can cover in both 3D and 2D the range of behavior between brittle and ductile when AQS simulations are used [36,41].

B. Equations of motion

Our goal is to analyze the effect of a finite shear rate on the brittle yielding transition observed in AQS conditions reported in Ref. [36]. To avoid adding too many ingredients at once, we study the dynamics at zero temperature in the absence of inertia. To this end, we perform molecular dynamics simulations using overdamped equations of motion at $T = 0$. We impose a simple shear flow in the $\hat{x}$ direction, where $\hat{x}$ is the unit vector along the x axis, and solve the following equations of motion:

$$\zeta\left(\frac{d\mathbf{r}_i}{dt} - \dot{\gamma}y_i\hat{x}\right) = -\sum_{j<k}\frac{\partial u(r_{jk}, d_{jk})}{\partial \mathbf{r}_i}, \tag{1}$$

where ζ is the viscous damping coefficient, $\mathbf{r}_i$ and y_i represent the position and its y component of a particle. We use Lees-Edwards boundary conditions to perform simulations at a finite shear strain rate $\dot{\gamma}$ [53].

In the absence of thermal fluctuations, the natural microscopic timescale is given by $\tau_0 = \zeta\bar{d}^2/\epsilon$, which controls the viscous dissipation of the system. Length, time, and energy are expressed in units of $\bar{d}$, τ_0, and ϵ, respectively. To integrate the equations of motion in Eq. (1), we employ the Runge-Kutta method of order 4 with a time step $\Delta t = 0.005$ and the Euler method with a time step $\Delta t = 0.001$ [54]. We confirmed that these two methods produce identical results. We compute the xy component of the stress, σ, using the Irving-Kirkwood formula.

Additionally, we perform strain-controlled AQS deformation using Lees-Edwards boundary conditions [40], to complement data obtained for the same model in Ref. [36]. The AQS shear method consists of a succession of tiny uniform shear deformation with a step size of $\Delta\gamma = 10^{-4}$ followed by energy minimization via the conjugate gradient method.
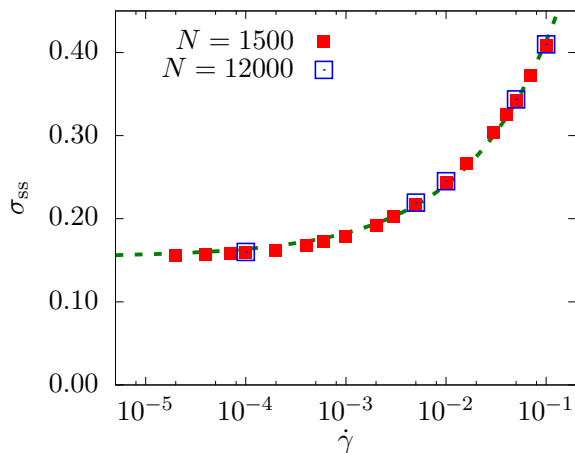
FIG. 1. Average shear stress in the steady state regime as a function of applied shear strain rate for the 3D with $N = 1500$ and $12\,000$. The green dashed curve represents the Herschel-Bulkley law with a yield stress independently measured in the AQS limit at $\dot{\gamma} = 0$.

By definition, the finite strain rate simulations described by Eq. (1) should produce results identical to the AQS simulations in the limit $\dot{\gamma} \to 0$. Therefore, Eq. (1) is the simplest and most natural extension of the AQS study of brittle yielding to finite strain rates, which introduces only one additional control parameter, $\dot{\gamma}$. In future work, it would be interesting to study the effect of temperature and of inertia on this phenomenon, which also introduce additional timescales in the problem.

III. MACROSCOPIC RHEOLOGY

A. Steady-state flow curve

Before showing results for the shear start-up setting, we present the steady-state flow curve to illustrate the range of $\dot{\gamma}$ that we impose, and the basic rheological properties of our numerical models at finite $\dot{\gamma}$ in the steady state, where no shear band is present. We check convergence to a steady state by monitoring the convergence of the potential energy to a stationary value. In practice, it is much faster to reach steady state starting from poorly annealed glasses.

In Fig. 1, we present the steady state flow curve for the 3D system and two system sizes, $N = 1500$ and $N = 12\,000$. The average of the shear stress in the steady state, σ_{ss}, is obtained by averaging over many configurations for strain larger than 1000% and over different samples. We do not observe finite size effects, at least down to $\dot{\gamma} = 10^{-4}$.

We independently measure the shear stress $\sigma_{ss}^{AQS} = 0.154$ in the steady state for the AQS condition. We substitute this value in the Herschel Bulkley equation [55], $\sigma_{ss} = \sigma_{ss}^{AQS} + B\dot{\gamma}^n$, where B is a prefactor, and find that this phenomenological equation describes our data very well with the exponent $n = 0.515$. This is within the range of the values ($n \approx 0.4 - 0.6$) reported for similar systems in several earlier studies [56–58].

In the steady state, we do not observe any instability, such as ordering along the shear direction, or shear localization. Besides, the obtained flow curve in Fig. 1 does not
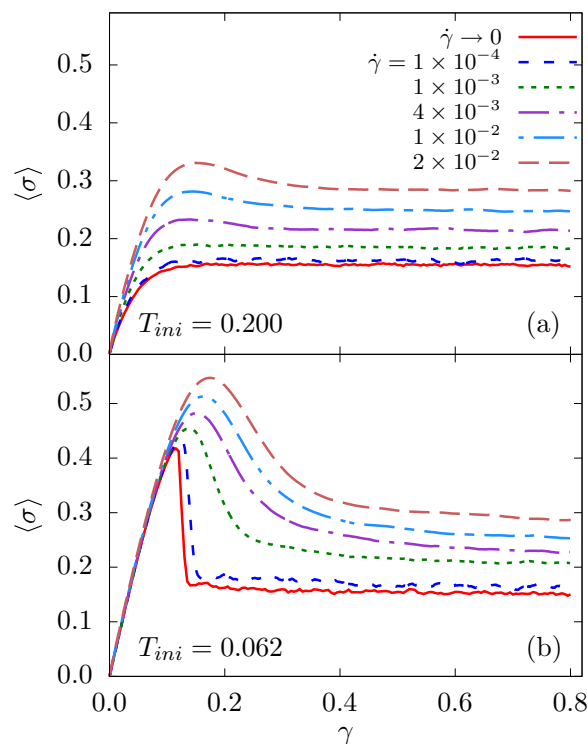

FIG. 2. Average stress strain curves for 3D glasses for $N = 12\,000$ (a) at high initial preparation temperature $T_{ini} = 0.200$ and (b) at low initial preparation temperature $T_{ini} = 0.062$. The data denoted $\dot{\gamma} \to 0$ are measured using AQS simulations.

present a nonmonotonic behavior. Thus, the system under study does not satisfy any known condition to produce permanent shear bands in the steady state [4,21,59]. In other words, the shear bands observed in our study in the shear start-up setting are inherently a transient phenomenon whose origin can directly be related to the nature of the initial configurations [16].

B. Shear start-up

We now focus on the macroscopic stress-strain curves obtained in the shear start-up setting. We prepare zero-temperature glasses at various depth in their energy landscape quantified by the preparation temperature T_{ini} and apply a finite shear rate at time $t = 0$. For each T_{ini}, we average the results over independent glass configurations to increase the statistics of the data to obtain the evolution of the average shear stress, denoted by $\langle \sigma \rangle$, as a function of the deformation $\gamma = \dot{\gamma}t$ since time $t = 0$. We present the results for poorly annealed glasses prepared at high temperature, $T_{ini} = 0.200$, and for very stable glasses prepared at low temperature, $T_{ini} = 0.062$.

In Fig. 2(a), we report the results for poorly annealed glasses. First, we show that in the AQS simulation, $\dot{\gamma} \to 0$, the system shows a completely monotonic crossover across yielding and reaches steady state without any stress overshoot, consistent with a very ductile behavior. When a finite strain rate is applied, deviations from the AQS results are clearly observed. As $\dot{\gamma}$ is increased, we observe that up to a strain rate $\dot{\gamma} \approx 10^{-3}$, the system shows a qualitatively similar monotonic

crossover to yielding, akin to the AQS conditions. Incrementing the strain rate further, $\dot{\gamma} \geqslant 4 \times 10^{-3}$, the system starts to present a stress overshoot during yielding [60,61]. The same trend can be observed for different system sizes from $N = 1500$ to 96 000.

It has been theoretically argued that the presence of the stress overshoot before reaching the steady state is associated with the emergence of shear banding [16]. However, a careful analysis of the nonaffine displacement field for these systems does not reveal any sign of a transient shear band in our simulations. Whereas shear bands may well appear at even larger system sizes [62], we feel that these systems are too ductile to show any interesting shear localization at such large shear rates.

In Fig. 2(b), we show the results obtained for very stable glasses. We find that all samples display a sharp shear band at low shear rates, which can be either horizontal or vertical. We average the stress strain curves over the samples showing horizontal shear bands to remove the small stress growth observed after yielding when a vertical shear band is present [38]. In this case, we observe that in the AQS limit the system shows a discontinuous stress drop after stress overshoot, as reported previously [36]. At finite but low strain rate, $\dot{\gamma} = 10^{-4}$, we observe that the average stress strain curve shows a trend very similar to the AQS results, with a very slight change of the slope $d\langle\sigma\rangle/d\gamma$ precisely at yielding as compared to the AQS limit. In that case, we also observe a system-spanning shear band, as discussed in more detail below in Sec. V. When the strain rate is increased further, $\dot{\gamma} \geqslant 10^{-3}$, the sharp stress drop at yielding is smeared out, and the corresponding slope is also systematically decreased. Concomitantly, the formation of a shear band is also altered, as described below in Sec. V.

For stable glasses, reaching the steady state requires straining the sample for extremely large values of γ. For example, $\gamma > 3.0$ is needed to reach the steady state at $\dot{\gamma} = 10^{-1}$ for $N = 12\,000$. Besides, the amount of strain to reach the steady state increases with increasing the system size or decreasing $\dot{\gamma}$. At the slowest shear rate limit, $\dot{\gamma} \rightarrow 0$, $\gamma = 10.0$ is not enough at all to reach the steady state for $N = 12\,000$ systems. Thus, the sheared glassy states obtained immediately after the stress overshoot in Fig. 2(b), say $0.6 \leqslant \gamma \leqslant 0.8$, are not yet typical of the steady state, even though the stress seems to have reached a stationary strain dependence. The energy is a more suitable observable to detect whether a steady state has been reached.

IV. YIELDING TRANSITION

Having exposed the basic phenomenology at finite strain rates in the previous section, we now focus on the effect of a finite $\dot{\gamma}$ on the nonequilibrium first-order transition observed in stable glasses in AQS simulations [36].

A. Finite size scaling analysis

In Fig. 3(a), we display stress strain curves for a stable glass in AQS simulations, varying the system size N. These data were first shown in Ref. [36]. The slope of these curves just after the stress overshoot becomes sharper with increasing
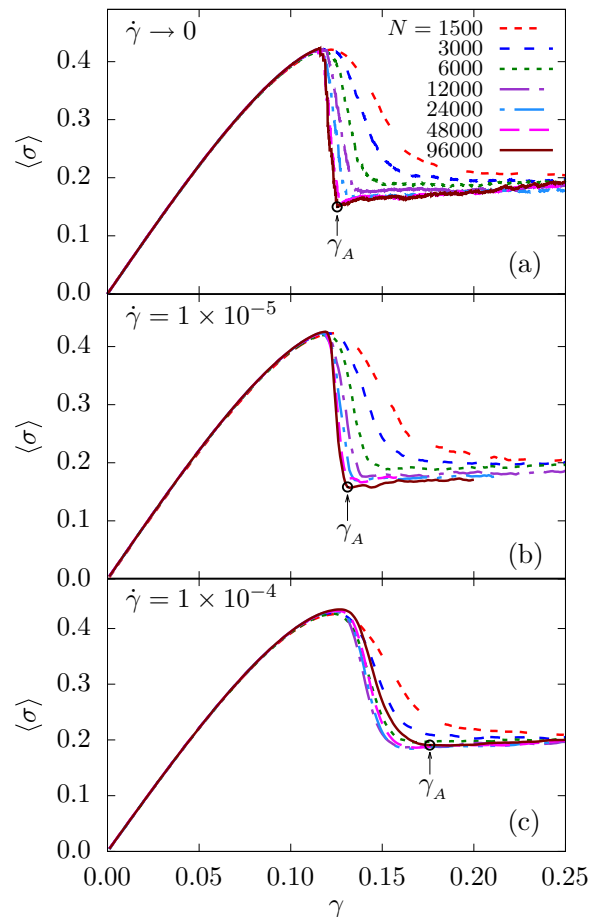

FIG. 3. Average stress strain curves for 3D AQS simulations (a), $\dot{\gamma} = 10^{-5}$ (b), and $\dot{\gamma} = 10^{-4}$ (c), and different system sizes. The preparation temperature is $T_{\text{ini}} = 0.062$. The vertical arrow indicates the location of γ_A used in Sec. V to study shear band formation.

system size, and the stress drop becomes a genuine discontinuity in the thermodynamic limit. Note that in Fig. 3 the slight increase of the stress observed after yielding stems from the fraction of samples where the shear band occurs in the vertical direction.

When a finite strain rate $\dot{\gamma} = 10^{-5}$ is applied for the same system sizes, see Fig. 3(b), the stress drop at yielding still gets increasingly sharper with system size, at least up to $N = 96\,000$. For these system sizes, then, we observe only little difference between this small shear rate and the AQS limit. However, when the strain rate is increased further, $\dot{\gamma} = 10^{-4}$, we observe that for $N \geqslant 12\,000$, the stress strain curves no longer evolve and the stress drop does not become sharper at larger N, see Fig. 3(c).

In summary, we find that for a finite strain rate, the sharp stress drop seen in the AQS limit initially gets sharper with increasing the system size, but there seems to exist a finite N above which it saturates. This crossover system size becomes larger for smaller shear rate, and presumably it diverges as $\dot{\gamma} \rightarrow 0$, so the AQS discontinuous limit is recovered. These observations suggest that the nonequilibrium first-order transition seen in the AQS simulation is now smeared out by the finite timescale introduced by the shear rate.
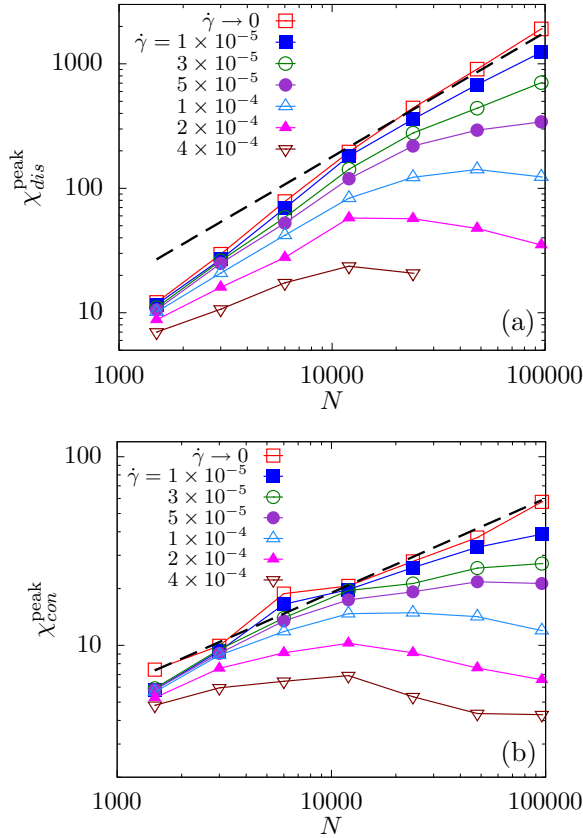
FIG. 4. The peak values of the disconnected (a) and connected (b) susceptibilities, $\chi_{\text{dis}}^{\text{peak}}$ and $\chi_{\text{con}}^{\text{peak}}$, as a function of the system size N for 3D stable glasses with $T_{\text{ini}} = 0.062$. The dashed lines correspond to the scaling behaviors observed in the AQS limit, $\chi_{\text{dis}}^{\text{peak}} \propto N$ and $\chi_{\text{con}}^{\text{peak}} \propto N^{1/2}$. Departure from the AQS limit arises at smaller N when $\dot{\gamma}$ increases, indirectly revealing a crossover lengthscale ξ controlled by the shear rate $\dot{\gamma}$.

B. Stress fluctuations and susceptibilities

In the AQS limit, the brittle yielding transition is most transparently revealed via the analysis of the stress fluctuations, which are efficiently quantified by two susceptibilities that we now discuss.

We first define the connected susceptibility,

$$\chi_{\text{con}} = -d\langle \sigma \rangle / d\gamma, \tag{2}$$

which can be directly measured from the derivative of the average stress strain curves shown in Fig. 3. The second quantity is the disconnected susceptibility,

$$\chi_{\text{dis}} = N(\langle \sigma^2 \rangle - \langle \sigma \rangle^2), \tag{3}$$

which quantifies the sample to sample fluctuations of the shear stress at a given strain γ. Both these susceptibilities exhibit a pronounced peak near yielding, and we define $\chi_{\text{con}}^{\text{peak}}$ and $\chi_{\text{dis}}^{\text{peak}}$ as the amplitude of these peaks. These amplitudes thus depend on the preparation temperature T_{ini}, on the system size N, and on the applied shear rate $\dot{\gamma}$.

In Fig. 4, we show the evolution of these peak values for 3D stable glasses with $T_{\text{ini}} = 0.062$. In the AQS limit, the system size dependence of the susceptibilities is well understood [36]. They both diverge as a power law of the system

size, $\propto N^\delta$ with $\delta = 1$ and $\delta = 1/2$ for the disconnected and connected susceptibilities, respectively. These divergences at $\dot{\gamma} \to 0$ reflect the existence of sharp nonequilibrium first-order transition in the thermodynamic limit [36].

When we apply a low finite $\dot{\gamma}$, at smaller N, $\chi_{\text{dis}}^{\text{peak}}$ and $\chi_{\text{con}}^{\text{peak}}$ still follow the AQS behavior for small enough N. However, they depart from the AQS behavior for larger N and the divergence with N is eventually avoided and replaced by a saturation of the fluctuations to a finite value. The deviations from the AQS limit become stronger with increasing the shear rate. These results confirm the existence of a crossover system size, $N^*(\dot{\gamma})$, below which the AQS behavior is observed, but above which the divergence of the stress fluctuations is cutoff. This crossover system size $N^*(\dot{\gamma})$ becomes larger for smaller shear rate, and it diverges in the AQS limit $\dot{\gamma} \to 0$.

These observations imply that there is a direct connection between the timescale imposed by the shear rate and a typical lengthscale $\xi = \xi(\dot{\gamma})$ characterizing the yielding transition. Since brittle yielding is associated with a single system spanning shear band, the crossover lengthscale revealed by the above analysis suggests the emergence of a characteristic lengthscale associated with shear band formation at finite shear rates, so a sharp behavior similar to AQS physics is observed when $L \ll \xi$, whereas a new physical regime is entered when $L \gg \xi$. This conclusion suggests that a direct visualization of the real-space deformations of yielding is needed, which is the topic of the next section.

V. A LENGTHSCALE ASSOCIATED WITH SHEAR BAND FORMATION

The purpose of this section is to analyze in real space how the sharp yielding transition observed in AQS conditions for stable glasses is modified when using a finite shear rate.

To this end, we spatially resolve the plastic activity by measuring the accumulated nonaffine displacement for each particle. We follow the standard method introduced by Falk and Langer to compute the quantity D_{min}^2, which provides the local deviation of the particle displacement from an affine deformation [63]. Particles with large D_{min}^2 typically belong to the shear band, whereas low plastic activity is revealed by a small D_{min}^2. At a given strain γ, we compute the deformation with respect to the unstrained sample at $\gamma = 0$. We also follow them [63] regarding the definition of neighboring particles and use a cutoff radius $r_{\text{cut}} = 2.5$.

A. Visualization in 3D

To best visualize the plastic activity in the strained samples, we need to choose a strain value very close to yielding, right after the stress drop that is observed in the macroscopic stress-strain curves. While this choice is easily made in the AQS limit where the stress drop in stable glasses is essentially instantaneous, this is less obvious at finite $\dot{\gamma}$. Typical choices are shown in Fig. 3. As seen in Fig. 3, for a given system size, γ_A should increase as $\dot{\gamma}$ increases. For example, for $N = 96\,000$, in the AQS limit this value is $\gamma_A \approx 0.125$, whereas at the strain rate $\dot{\gamma} = 10^{-5}$ and $\dot{\gamma} = 10^{-4}$ take $\gamma_A \approx 0.130$ and $\gamma_A \approx 0.176$, respectively. All the images shown below are for the largest system simulated in 3D, $N = 96\,000$.
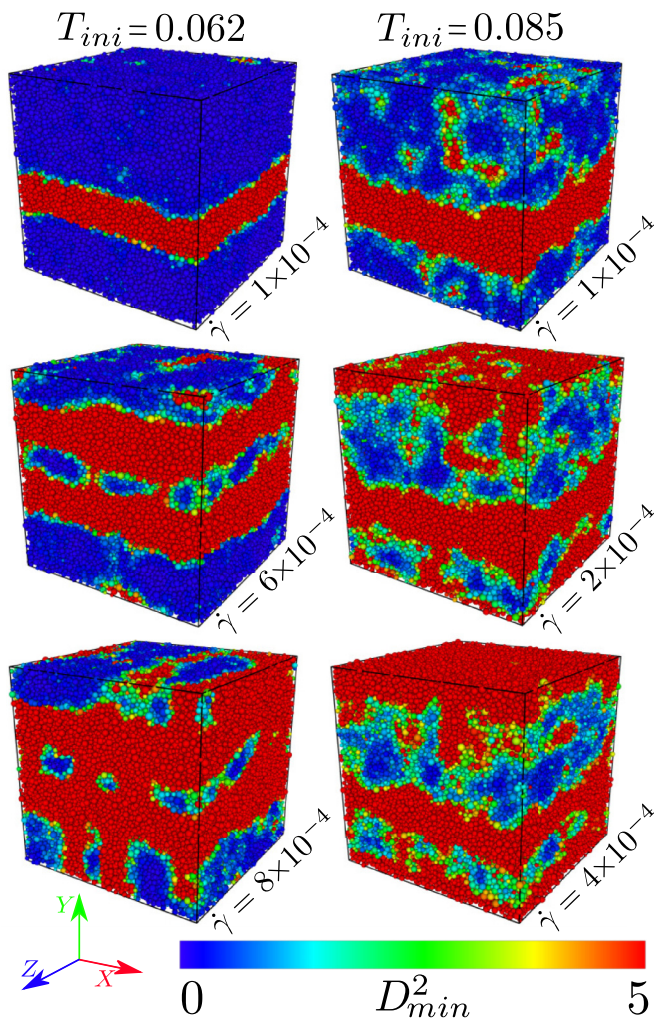
FIG. 5. Snapshots of the nonaffine $D_{\min}^2$ field immediately after yielding (at the strain γ_A shown in Fig. 3) for two different T_{ini} and various shear rates $\dot{\gamma}$ for the 3D system with $N = 96\,000$. An increasing number of shear bands is observed as the strain rate increases.

We summarize our observations in Fig. 5, which shows snapshots for different $\dot{\gamma}$ at the corresponding γ_A for glasses prepared initially at $T_{ini} = 0.062$ and $T_{ini} = 0.085$. Both preparation temperatures are below the brittle-to-ductile critical temperature of the AQS condition, $T_{ini,c} \approx 0.095$, and thus show sharp discontinuous stress drops in AQS simulations [36].

First, we discuss the results for the best annealed sample ($T_{ini} = 0.062$). Whereas we have observed smearing out of the sharp stress drop at a rate of $\dot{\gamma} = 1 \times 10^{-4}$ (see Fig. 3), the system still forms a well-defined single shear band right after yielding. As we increase the strain rate to $\dot{\gamma} = 6 \times 10^{-4}$, two shear bands are typically observed, with additional smaller plastic events seen elsewhere in the system. Increasing even further the strain rate to $\dot{\gamma} = 8 \times 10^{-4}$, we now observe multiple shear bands in both horizontal and vertical directions. A qualitatively similar behavior is observed for $T_{ini} = 0.085$, but many more plastic events are already present at the smallest shear rate $\dot{\gamma} = 1 \times 10^{-4}$, which coexist with a macroscopic shear band. Again, increasing the shear

rate results in multiple shear bands that are less and less well-resolved.

Our numerical results, where the unique control parameter is the increasing shear rate should be interpreted as follows. When $\dot{\gamma}$ is finite, the system does not have enough time to develop a single system-spanning shear band. Instead, it responds to the applied strain by independently forming several shear bands at various locations in the material [47]. We notice that the emergence of multiple shear bands at high loading rates has also been reported in metallic and silica glass experiments in various loading conditions, compressive [42,44,64,65], tensile [46,47], and nanoindentation [45] deformation tests, as well as molecular dynamics simulations [48]. We discuss these results further in Sec. VI.

B. Visualization in 2D

From the above real-space observations in 3D, we concluded that an increasing strain rate produces multiple shear bands, suggesting that a typical finite distance, ξ, between shear bands emerges at finite $\dot{\gamma}$, and decreases at larger $\dot{\gamma}$. We postulate that this is a relevant lengthscale for the yielding transition, that we wish to characterize further.

It is however difficult to quantify this length scale from the simulations shown in Fig. 5 because the system size remains too small, despite the fact that we use $N = 96\,000$ particles, which corresponds to a linear system size $L = 45.5$. To overcome this difficulty, we perform a similar analysis in 2D systems. This allows us to access larger linear sizes ($L = 253$ for $N = 64\,000$), and thus to quantitatively determine how the lengthscale ξ varies with $\dot{\gamma}$. The AQS limit for the 2D model is studied more carefully in Ref. [41].

As in 3D, we vary the initial stability of the glass samples by changing T_{ini} over a considerable range, from very stable glasses to poorly annealed materials to highlight the nature of the measured lengthscale ξ. In particular, we wish to discriminate ξ from previously reported lengthscales in the literature, discussed in the steady state or poorly annealed materials [66,67].

We again analyze the configurations of the 2D systems at the strain value immediately after the stress overshoot γ_A. For a given $\dot{\gamma}$, γ_A depends very little on T_{ini} (within 5%) and therefore we choose the same γ_A irrespective of T_{ini}. We use $\gamma_A = 0.070$, 0.107, 0.125, 0.150, and 0.190, for $\dot{\gamma} \to 0$ (AQS), $\dot{\gamma} = 10^{-5}$, 10^{-4}, 10^{-3}, and 10^{-2}, respectively.

We summarize our results in the snapshots shown in Fig. 6 where several strain rates and preparation temperatures are shown. Starting with the AQS limit (top row), we observe homogeneous plastic activity for poorly annealed systems, and a gradual emergence of shear localization as T_{ini} is decreased, followed by a single sharp shear band at low T_{ini}. This evolution mirrors the physics observed in 3D AQS simulations [36], and its nature is discussed further in Ref. [41]. We find that there is a critical preparation temperature $T_{ini,c} \approx 0.1$ separating brittle and ductile yielding behaviors also in two dimensions [41]. For T_{ini} close to $T_{ini,c}$, the snapshots reveal a combination of randomly distributed plastic events and a system-spanning shear band.

When $\dot{\gamma}$ is increased from $\dot{\gamma} = 10^{-5}$ to $\dot{\gamma} = 10^{-2}$, for poorly annealed samples at $T_{ini} = 0.200$, the plastic
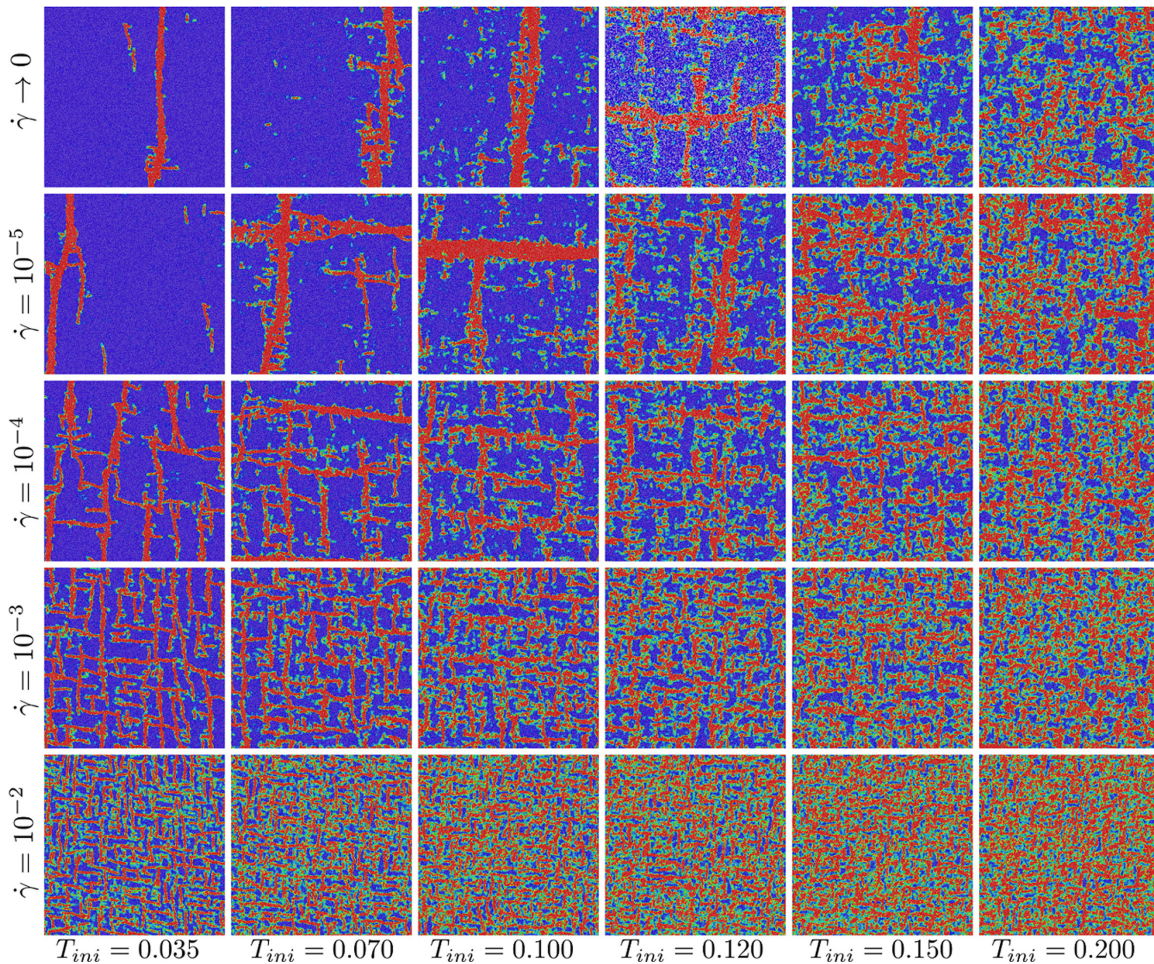
FIG. 6. Snapshots of the nonaffine D_{min}^2 field immediately after yielding (at the strain γ_A) for several T_{ini} and various shear rates $\dot{\gamma}$ for the 2D system with $N = 64\,000$ ($L = 253$). An increasing number of shear bands are formed as the strain rate increases, which form a checkerboard pattern for low T_{ini} with characteristic lengthscale $\langle \xi \rangle$.

rearrangements continue to fill the entire sample and remain homogeneously distributed in space. The shear rate plays only a minor role in these snapshots, the contrast between regions with large and small nonaffine displacements become less pronounced as $\dot{\gamma}$ increases. Despite the existence of a stress drop in the average stress-strain curves, these samples do not display shear localization.

On the other hand, for stable glass samples at $T_{ini} = 0.035$, multiple shear bands appear in both horizontal and vertical directions, as seen for instance for $\dot{\gamma} = 10^{-4}$. This result is similar to the above observations in 3D. Although less striking, it also appears that the width of each shear band becomes thinner at larger shear rate [68]. As $\dot{\gamma}$ is increased further for the stable glasses, the density of shear bands increases, or, equivalently, the typical distance between two shear bands decreases. When several shear bands appear inside the system, they form a sort of "checkerboard" structure (see, for instance, $\dot{\gamma} = 10^{-3}$ and $\dot{\gamma} = 10^{-2}$). Finally, the samples at intermediate temperatures, $T_{ini} = 0.070 - 0.150$, appear as a superposition of the two extreme cases ($T_{ini} = 0.035$ and 0.200), with homogeneously spread plastic activity superposed to a checkerboard pattern.

C. A shear-rate-dependent lengthscale for shear banding

To quantify the typical distance between two shear bands which would be the relevant lengthscale associated with shear band formation in the system, we first compute D_{min}^2 for each particle. This quantity, however, takes continuous values. We first transform it into a binary variable to more clearly distinguish the shear bands from the rest of the system. We use a threshold value $D_{min}^2 = 2.0$, below which we consider the region as being outside the shear band. This binary field now clearly specifies the interface separating the two regions. We checked that transforming the snapshots in Fig. 6 using the binary field leaves the images essentially unaffected.

This binary information can then be used to compute the typical lengthscale between the shear bands, by measuring the chord length distribution, recording distances between the shear bands. We define a chord by two consecutive intersections of a straight line with the non-shear-band region present in the system [69]. To gather statistics, we draw many straight lines in both x and y directions, taking care of the Lees-Edwards boundary conditions, and measure the length ξ of each chord along each straight line. We therefore measure for each configuration a distribution of chord lengths, $P(\xi)$.
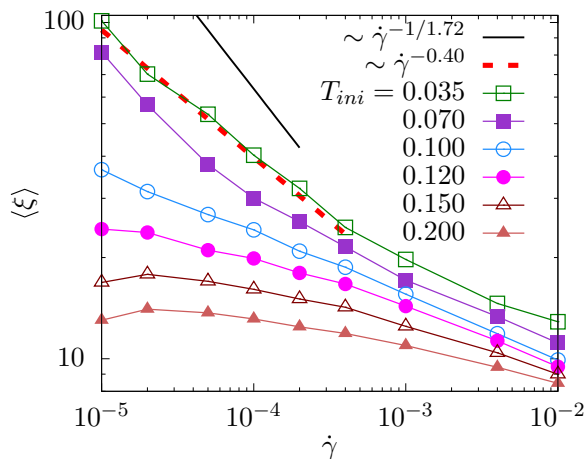
FIG. 7. Evolution of the typical distance between shear bands with the shear rate for the 2D model at various values of $T_{\rm ini}$. The solid straight line corresponds to the scaling predicted by Eq. (7) using the exponent $\beta = 1.72$ measured in Fig. 8, which should hold for low $T_{\rm ini}$ and small $\dot{\gamma}$. The dashed straight line corresponds to the fitting by Eq. (5) with the exponent $\alpha = 0.4$.

We can then define an average distance between shear bands as the first moment of this distribution:

$$\langle \xi \rangle = \int_0^\infty d\xi' P(\xi')\xi'. \tag{4}$$

By construction, $\langle \xi \rangle$ should thus quantitatively represent the typical size of the checkerboard patterns shown in Fig. 6. This lengthscale characterizing yielding has a very different nature from lengthscales reported previously, such as the typical distance between plastic events measured in the steady state [66,67].

We show in Fig. 7 the evolution of the measured $\langle \xi \rangle$ as a function of $\dot{\gamma}$ for the entire range of $T_{\rm ini}$ analyzed in 2D. Stable glasses at $T_{\rm ini} = 0.035$ and 0.070 show monotonic growth of $\langle \xi \rangle$ with decreasing $\dot{\gamma}$, as expected from the direct visualization in Fig. 6. For these stable glasses, $\langle \xi \rangle$ seems to grow algebraically at low shear rate,

$$\langle \xi \rangle \propto \dot{\gamma}^{-\alpha}, \tag{5}$$

with $\alpha \approx 0.4$, suggesting that the distance between shear bands indeed diverges in the AQS limit $\dot{\gamma} \to 0$. This divergence implies that a single shear band exists in fully AQS simulations in the thermodynamic limit.

On the other hand, for less well-annealed glasses, especially $T_{\rm ini} = 0.150$ and 0.200, the lengthscale $\langle \xi \rangle$ saturates at small $\dot{\gamma}$ to a finite value, suggesting that these systems exhibit a homogeneous spatial distribution of plastic events at large scales, $L \gg \langle \xi \rangle$. Interestingly, glass samples prepared near the critical point, $T_{\rm ini,c} \approx 0.1$ seem to also exhibit a power law divergence with $\dot{\gamma}$, albeit with a different exponent α. It would be interesting to relate this exponent to the criticality discussed in Ref. [36]. We also anticipate that $\langle \xi \rangle(\dot{\gamma}, T_{\rm ini})$ may obey a form of critical scaling as a function of the distance $\Delta T = |T_{\rm ini} - T_{\rm ini,c}|$. Our data remain insufficient to study these critical behaviours.

More broadly, these results suggest that the lengthscale $\langle \xi \rangle$ introduced above may provide a quantitative definition of the

degree of ductility; very ductile yielding being characterized by a very small $\langle \xi \rangle$, whereas brittle ones would exhibit a large value of $\langle \xi \rangle$. In this view, the sharp yielding transition at $\dot{\gamma} \to 0$ corresponds to $\langle \xi \rangle \to \infty$.

D. Physical interpretation and scaling argument

We first argue that the typical lengthscale between shear bands, $\langle \xi \rangle$, can be used to assess finite size effects. For $L < \langle \xi \rangle$, a single system-spanning shear band is observed in the simulated system, whereas multiple shear bands appear for $L > \langle \xi \rangle$. This reasoning directly explains the system size dependence of the susceptibilities shown in Fig. 4, since stress fluctuations should saturate when the system size becomes larger than $\langle \xi \rangle$.

Furthermore, the observed scaling behavior, $\langle \xi \rangle \propto \dot{\gamma}^{-\alpha}$, can be physically interpreted as follows. In AQS simulations, the system is given an infinite amount of time to relax in the nearest energy minimum after each strain increment. In practice, this energy minimization takes of course a finite amount of time since the system size is always finite and an efficient conjugate gradient algorithm is employed. Thus, it is possible to observe a unique system-spanning shear band even when the system size increases, $L \to \infty$ (and hence the timescale for shear band formation increases). When a finite shear rate is imposed, however, the shear band only reaches a given size before the external deformation can trigger another shear band elsewhere in the material. Let us define $\tau_{\rm SB}(L)$ the typical timescale for a single shear band to develop inside a system of finite linear size, L. If we assume that this timescale grows with the system size as

$$\tau_{\rm SB} \propto L^\beta, \tag{6}$$

then it follows that in a very large system deformed at a finite strain rate, the typical distance between the shear bands should scale as

$$\langle \xi \rangle \propto \dot{\gamma}^{-1/\beta}, \tag{7}$$

which suggests a relation between the exponent α introduced in Eq. (5) and the exponent β characterizing the dynamics of shear band formation in Eq. (6), namely,

$$\alpha = 1/\beta. \tag{8}$$

To test these ideas, we estimate $\tau_{\rm SB}$ by direct numerical simulations. To this end, we first perform AQS simulations of stable glasses for which a system-spanning shear band forms at yielding accompanying the largest stress drop. In AQS simulations, the stress relaxation is realized by the energy minimization procedure which uses some unphysical dynamics (such as the conjugate gradient method [51] or FIRE algorithm [70]) to reach the energy minimum as quickly as possible. To measure the timescale $\tau_{\rm SB}$, we perform AQS simulations up to the last step before the largest stress drop, but we then switch to the physically steepest descent dynamics described by Eq. (1) at zero strain rate. Thus the system now obeys the physically correct dynamics during the largest stress drop, which allows us to numerically observe the formation of the shear band.

In Fig. 8(a), we show the typical time evolution of the stress, $\sigma(t)$, during the largest stress drop when the steepest
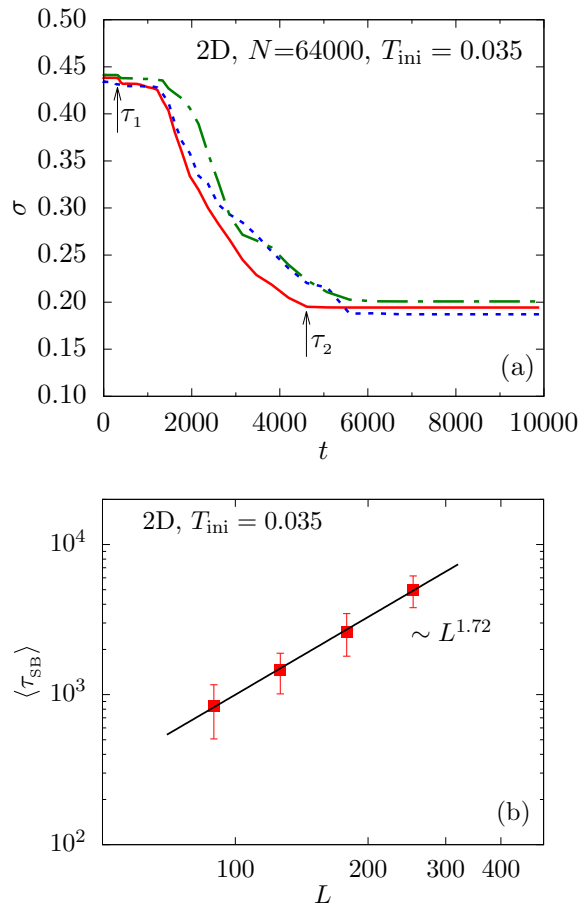
FIG. 8. (a) Stress relaxation during the largest stress drop for stable glasses using the physically steepest descent dynamics. The times τ_1 and τ_2 describe the beginning and the end of the shear band formation for the red curve. (b) The averaged duration of the shear band formation, $\langle \tau_{SB} \rangle = \langle \tau_2 - \tau_1 \rangle$ increases algebraically with the system size with an exponent $\beta \approx 1.72$ that is then used in Fig. 7.

descent dynamics is employed for 2D systems with $N = 64\,000$ and $T_{ini} = 0.035$. We show three independent samples. We define $\tau_{SB} = \tau_2 - \tau_1$, where τ_1 and τ_2 are the times when $\sigma(t)$ drops 1% below $\sigma(0)$ and when $\sigma(t)$ reaches 1% above $\sigma(\infty)$. These two timescales represent roughly the beginning and the end of the shear band formation, as specified by the arrows in Fig. 8(a). Therefore, τ_{SB} quantifies the duration of the formation of a system-spanning shear band in a system of finite size L.

We repeat this analysis for many samples (respectively, 49, 68, 76, and 73, for $N = 8000$, $16\,000$, $32\,000$, and $64\,000$), from which we deduce the average value $\langle \tau_{SB} \rangle$. We then repeat these measurements for various system sizes to estimate how the timescale for the formation of a system-spanning shear band grows with the linear size of the system. The results are displayed in Fig. 8(b). Within the error bars, we find that $\langle \tau_{SB} \rangle \propto L^\beta$ with $\beta \approx 1.72$. This value for the exponent β translates into an exponent $\alpha \approx 1/1.72 \approx 0.58$, which is not far from (but certainly larger than) our numerical observations $\alpha \approx 0.4$ in Fig. 7, although the predicted scaling for $\langle \xi \rangle$ overestimates somewhat the measured growth of the lengthscale. This can be attributed to the fact that

the checkerboard patterns in Fig. 6 contain very small shear bands that may bias the chord length distribution toward smaller lengthscales. We expect our prediction to become better when sharp, large shear bands exist, i.e., when both the shear rate $\dot{\gamma}$ and the preparation temperature T_{ini} are small. This trend is compatible with the data shown in Fig. 7.

Therefore, our independent analysis supports the idea that the lengthscale $\langle \xi \rangle$ and its scaling with the shear rate result from the competition between the timescale for the formation of a shear band and the imposed shear rate. The degree of brittleness of yielding thus decreases continuously with the imposed shear rate.

We have repeated the same timescale analysis for the most stable system with $T_{ini} = 0.062$ in 3D. We again approach the macroscopic stress drop using AQS simulations, but we simulate the largest stress drop dynamics using the physically steepest dynamics. Repeating this analysis for different system sizes, we estimate that the exponent β in Eq. (6) is $\beta \approx 0.96$ in 3D, suggesting that the exponent β and hence $\alpha = 1/\beta \approx 1.04$ may depend somewhat on the spatial dimension. Clearly, more work is needed to assess more precisely the value of this exponent, and to understand better the kinetics of the formation of shear bands in amorphous materials since our 2D and 3D data do not allow us to distinguish between diffusive ($\beta = 2$) or ballistic ($\beta = 1$) propagation of the shear band. While we may expect that shear bands form ballistically as the macroscopic avalanche unfolds, as we observe here in 3D, our AQS simulations in 2D have revealed the presence of strong spatial disorder-induced fluctuations [41] that may explain the slower shear-band propagation (and thus the larger exponent β) obtained above. We leave this issue for future work.

VI. DISCUSSION AND PERSPECTIVES

We have numerically studied the effect of using a finite strain rate on the yielding of model glasses prepared over a very wide range of initial stabilities. We found that the nonequilibrium discontinuous transition observed in the AQS conditions for stable glasses [36] is smeared out when a finite deformation rate $\dot{\gamma}$ is imposed. In the quasistatic limit, stable glasses yield at a well-defined yield strain value via the formation of a unique system-spanning shear band because the first shear band that appears in the system can propagate throughout the material before the next plastic event occurs. Instead, at finite shear rates, several shear bands can form independently in the material and propagate over a finite lengthscale $\langle \xi \rangle$ that decays algebraically with the shear rate. Therefore, the sharp difference between the yielding transitions of poorly-annealed and stable glasses obtained in the quasistatic limit is blurred at finite shear rates where both types of materials display smooth yielding transitions. Yet, the lengthscale $\langle \xi \rangle$ reveals the difference between these two types of materials, since stable systems are characterized by a large distance between localized shear bands (and thus a large value of $\langle \xi \rangle$ that grows when the shear rate is decreased) whereas poorly annealed glasses display a more homogeneous map of plastic activity (and thus have a small, $\dot{\gamma}$-independent value of $\langle \xi \rangle$).

Our results open some interesting avenues for future research. It would be interesting to understand and better characterize the lengthscale $\langle\xi\rangle$ in various theoretical settings, from atomistic simulations in various glassy models to more coarse-grained descriptions such as elastoplastic models where larger system sizes can more easily be studied, in particular perhaps in 3D. More generally, our work should motivate theoretical models, such as soft glassy rheology [16], shear transformation zone [68], elastoplastic models [31], mode-coupling theory [71] and random first-order transition theory [72,73] to address the problem of brittle yielding at finite shear rates.

Moreover, our results suggest many directions for future computer simulations along the lines proposed here. It would be interesting to study the effect of dimensionality [41], temperature, and inertia in more details. It would also be important to study other loading conditions, such as cyclic shear [74–76] and extensional flows to assess the generality of our results. In particular, it has been reported that ductility increases with increasing the shear rate in tensile experiments [46,47] (as we observed numerically), whereas compression tests have demonstrated the same [64] and the opposite trend [42,44], depending on geometrical constraint of mechanical apparatus. Besides, recent silica glass compression tests using a very wide range of strain rate have reported the nonmonotonic dependence of ductility on the loading rate [65]. Notably, this experiment has revealed that the ductility increases with increasing the strain rate at a very high rate regime covered by computer simulations. Although the emergence of the multiple shear bands and higher loading rate are positively correlated in general, its relation with ductility is a delicate problem, which might be affected by other factors such as how the stress spreads and accumulates in the macroscopic structure of the system. More generally, it now becomes possible to simulate the formation of shear bands in amorphous solids with stability comparable to the ones of metallic and silica glasses. It thus becomes possible to understand the details of the kinetic mechanism of shear-band formation in these systems at the atomic scale.

[1] J.-L. Barrat and A. Lemaitre, Dyn. Heterogeneities Glasses, Colloids, Granular Media **150**, 264 (2011).

[2] D. Rodney, A. Tanguy, and D. Vandembroucq, Modell. Simul. Mater. Sci. Eng. **19**, 083001 (2011).

[3] M. L. Falk and J. S. Langer, Annu. Rev. Condens. Matter Phys. **2**, 353 (2011).

[4] D. Bonn, M. M. Denn, L. Berthier, T. Divoux, and S. Manneville, Rev. Mod. Phys. **89**, 035005 (2017).

[5] A. Nicolas, E. E. Ferrero, K. Martens, and J.-L. Barrat, Rev. Mod. Phys. **90**, 045006 (2018).

[6] A. Greer, Y. Cheng, and E. Ma, Mater. Sci. Eng., R **74**, 71 (2013).

[7] J. Schroers and W. L. Johnson, Phys. Rev. Lett. **93**, 255506 (2004).

[8] J. Lu, G. Ravichandran, and W. L. Johnson, Acta Mater. **51**, 3429 (2003).

[9] Y. Yang and C. T. Liu, J. Mater. Sci. **47**, 55 (2012).

[10] C. H. Scholz, *The Mechanics of Earthquakes and Faulting* (Cambridge University Press, Cambridge, 2019).

[11] M. Popović, T. W. de Geus, and M. Wyart, Phys. Rev. E **98**, 040901(R) (2018).

[12] Y. Shi and M. L. Falk, Phys. Rev. Lett. **95**, 095502 (2005).

[13] J. Rottler and M. O. Robbins, Phys. Rev. Lett. **95**, 225504 (2005).

[14] G. Kumar, P. Neibecker, Y. H. Liu, and J. Schroers, Nat. Commun. **4**, 1536 (2013).

[15] M. Fan, M. Wang, K. Zhang, Y. Liu, J. Schroers, M. D. Shattuck, and C. S. O'Hern, Phys. Rev. E **95**, 022611 (2017).

[16] R. L. Moorcroft, M. E. Cates, and S. M. Fielding, Phys. Rev. Lett. **106**, 055502 (2011).

[17] M. Vasoya, C. H. Rycroft, and E. Bouchbinder, Phys. Rev. Appl. **6**, 024008 (2016).

[18] Y. Jin and H. Yoshino, Nat. Commun. **8**, 14935 (2017).

[19] A. Tanguy, F. Leonforte, and J.-L. Barrat, Eur. Phys. J. E **20**, 355 (2006).

[20] G. P. Shrivastav, P. Chaudhuri, and J. Horbach, Phys. Rev. E **94**, 042605 (2016).

[21] S. M. Fielding, Rep. Prog. Phys. **77**, 102601 (2014).

[22] S. Karmakar, E. Lerner, and I. Procaccia, Phys. Rev. E **82**, 055103(R) (2010).

[23] K. M. Salerno, C. E. Maloney, and M. O. Robbins, Phys. Rev. Lett. **109**, 105703 (2012).

[24] J. Lin, E. Lerner, A. Rosso, and M. Wyart, Proc. Natl. Acad. Sci. USA **111**, 14382 (2014).

[25] N. Koumakis, M. Laurati, S. U. Egelhaaf, J. F. Brady, and G. Petekidis, Phys. Rev. Lett. **108**, 098303 (2012).

[26] A. Ghosh, Z. Budrikis, V. Chikkadi, A. L. Sellerio, S. Zapperi, and P. Schall, Phys. Rev. Lett. **118**, 148001 (2017).

[27] M. L. Manning and A. J. Liu, Phys. Rev. Lett. **107**, 108302 (2011).

[28] S. Patinet, D. Vandembroucq, and M. L. Falk, Phys. Rev. Lett. **117**, 045501 (2016).

[29] E. D. Cubuk, R. Ivancic, S. S. Schoenholz, D. Strickland, A. Basu, Z. Davidson, J. Fontaine, J. L. Hor, Y.-R. Huang, Y. Jiang *et al.*, Science **358**, 1033 (2017).

[30] R. Dasgupta, H. G. E. Hentschel, and I. Procaccia, Phys. Rev. E **87**, 022810 (2013).

[31] C. Liu, E. E. Ferrero, F. Puosi, J.-L. Barrat, and K. Martens, Phys. Rev. Lett. **116**, 065501 (2016).

[32] C. Rainone, P. Urbani, H. Yoshino, and F. Zamponi, Phys. Rev. Lett. **114**, 015701 (2015).

[33] A. Wisitsorasak and P. G. Wolynes, Proc. Natl. Acad. Sci. USA **109**, 16068 (2012).

[34] P. Urbani and F. Zamponi, Phys. Rev. Lett. **118**, 038001 (2017).

[35] P. K. Jaiswal, I. Procaccia, C. Rainone, and M. Singh, Phys. Rev. Lett. **116**, 085501 (2016).

[36] M. Ozawa, L. Berthier, G. Biroli, A. Rosso, and G. Tarjus, Proc. Natl. Acad. Sci. USA **115**, 6656 (2018).

[37] A. Ninarello, L. Berthier, and D. Coslovich, Phys. Rev. X **7**, 021039 (2017).

[38] G. Kapteijns, W. Ji, C. Brito, M. Wyart, and E. Lerner, Phys. Rev. E **99**, 012106 (2019).

[39] S. K. Nandi, G. Biroli, and G. Tarjus, Phys. Rev. Lett. **116**, 145701 (2016).

[40] C. E. Maloney and A. Lemaître, Phys. Rev. E **74**, 016118 (2006).

[41] M. Ozawa, L. Berthier, G. Biroli, and G. Tarjus, arXiv:1912.06021.

[42] J. Antonaglia, X. Xie, G. Schwarz, M. Wraith, J. Qiao, Y. Zhang, P. K. Liaw, J. T. Uhl, and K. A. Dahmen, Sci. Rep. **4**, 4382 (2014).

[43] C. P. Amann, M. Siebenbürger, M. Krüger, F. Weysser, M. Ballauff, and M. Fuchs, Journal of Rheology **57**, 149 (2013).

[44] T. Mukai, T. Nieh, Y. Kawamura, A. Inoue, and K. Higashi, Intermetallics **10**, 1071 (2002).

[45] C. Schuh and T. Nieh, Acta Mater. **51**, 87 (2003).

[46] A. V. Sergueeva, N. Mara, D. Branagan, and A. Mukherjee, Scr. Mater. **50**, 1303 (2004).

[47] K. Hajlaoui, M. Stoica, A. LeMoulec, F. Charlot, and A. Yavari, Rev. Adv. Mater. Sci. **18**, 23 (2008).

[48] M. Wakeda, Y. Shibutani, S. Ogata, and J. Park, Appl. Phys. A **91**, 281 (2008).

[49] G. Parisi, I. Procaccia, C. Rainone, and M. Singh, Proc. Natl. Acad. Sci. USA **114**, 5577 (2017).

[50] L. Berthier, D. Coslovich, A. Ninarello, and M. Ozawa, Phys. Rev. Lett. **116**, 238002 (2016).

[51] J. Nocedal and S. Wright, *Numerical Optimization* (Springer Science & Business Media, 2006).

[52] L. Berthier, P. Charbonneau, A. Ninarello, M. Ozawa, and S. Yaida, Nat. Commun. **10**, 1508 (2019).

[53] M. P. Allen and D. J. Tildesley, *Computer Simulation of Liquids* (Oxford University Press, New York, 1989).

[54] D. Frenkel and B. Smit, *Understanding Molecular Simulation: From Algorithms to Applications* (Academic Press, San Diego, 2002).

[55] W. H. Herschel and R. B. Bulkley, Kolloid Z. **39**, 291 (1926).

[56] A. Ikeda, L. Berthier, and P. Sollich, Phys. Rev. Lett. **109**, 018301 (2012).

[57] V. V. Vasisht, S. K. Dutta, E. Del Gado, and D. L. Blair, Phys. Rev. Lett. **120**, 018001 (2018).

[58] R. Cabriolu, J. Horbach, P. Chaudhuri, and K. Martens, Soft Matter **15**, 415 (2019).

[59] K. Martens, L. Bocquet, and J.-L. Barrat, Soft Matter **8**, 4197 (2012).

[60] F. Varnik, L. Bocquet, and J.-L. Barrat, J. Chem. Phys. **120**, 2788 (2004).

[61] M. Tsamados, Eur. Phys. J. E **32**, 165 (2010).

[62] V. V. Vasisht, M. L. Goff, K. Martens, and J.-L. Barrat, arXiv:1812.03948.

[63] M. L. Falk and J. S. Langer, Phys. Rev. E **57**, 7192 (1998).

[64] A. Sergueeva, N. Mara, J. Kuntz, E. Lavernia, and A. Mukherjee, Philos. Mag. **85**, 2671 (2005).

[65] R. Ramachandramoorthy, J. Schwiedrzik, L. Petho, C. Guerra-Nuñez, D. Frey, J.-M. Breguet, and J. Michler, Nano Lett. **19**, 2350 (2019).

[66] A. Lemaître and C. Caroli, Phys. Rev. Lett. **103**, 065501 (2009).

[67] S. Karmakar, E. Lerner, I. Procaccia, and J. Zylberg, Phys. Rev. E **82**, 031301 (2010).

[68] M. L. Manning, E. G. Daub, J. S. Langer, and J. M. Carlson, Phys. Rev. E **79**, 016110 (2009).

[69] V. Testard, L. Berthier, and W. Kob, Phys. Rev. Lett. **106**, 125702 (2011).

[70] E. Bitzek, P. Koskinen, F. Gähler, M. Moseler, and P. Gumbsch, Phys. Rev. Lett. **97**, 170201 (2006).

[71] J. M. Brader, T. Voigtmann, M. Fuchs, R. G. Larson, and M. E. Cates, Proc. Natl. Acad. Sci. USA **106**, 15186 (2009).

[72] A. Wisitsorasak and P. G. Wolynes, Proc. Natl. Acad. Sci. USA **114**, 1287 (2017).

[73] E. Agoritsas, T. Maimbourg, and F. Zamponi, J. Phys. A: Math. Theor. **52**, 144002 (2019).

[74] W.-T. Yeh, M. Ozawa, K. Miyazaki, T. Kawasaki, and L. Berthier, arXiv:1911.12951.

[75] N. V. Priezjev, arXiv:1911.06157.

[76] H. Bhaumik, G. Foffi, and S. Sastry, arXiv:1911.12957.